Solar-to-fuels conversion over In_2O_3/g-C_3N_4 hybrid photocatalysts

Shao-Wen Cao [a], Xin-Feng Liu [b], Yu-Peng Yuan [a,c], Zhen-Yi Zhang [a], Yu-Sen Liao [a], Jun Fang [a], Say Chye Joachim Loo [a,*], Tze Chien Sum [b], Can Xue [a,*]

[a] Solar Fuels Lab, School of Materials Science and Engineering, Nanyang Technological University, Singapore 639798, Singapore
[b] Division of Physics and Applied Physics, School of Physical of Mathematical Sciences, Nanyang Technological University, Singapore 637371, Singapore
[c] Laboratory of Advanced Porous Materials, School of Chemistry and Chemical Engineering, Anhui University, Hefei 230039, PR China

ARTICLE INFO

ABSTRACT

We have achieved in-situ growth of In_2O_3 nanocrystals onto the sheet-like g-C_3N_4 surface. The resulting In_2O_3–g-C_3N_4 hybrid structures exhibit considerable improvement on the photocatalytic activities for H_2 generation and CO_2 reduction. The enhanced activities are attributed to the interfacial transfer of photogenerated electrons and holes between g-C_3N_4 and In_2O_3, leading to effective charge separation on both parts. Further studies by transient PL spectroscopy confirm that the In_2O_3–g-C_3N_4 heterojunctions remarkably promote the charge transfer efficiency, thereby increase the charge carrier lifetime for the photocatalytic reactions.

© 2013 Elsevier B.V. All rights reserved.

1. Introduction

The fuels production through solar-driven water splitting or CO_2 reduction has been considered as a promising way to solve the worldwide energy shortage [1–3]. In the past decade, great efforts have been made to explore solar-to-fuel conversion by using various semiconductor photocatalysts including TiO_2 [4,5], Cu_2O [6,7], $SrTiO_3$ [8,9], $ZnFe_2O_4$ [10], CdS [11,12], $InVO_4$ [13] etc. Among them, In_2O_3 is known as a semiconductor with an indirect bandgap of ~2.8 eV, and has been proved as a visible-light-active photocatalyst [14,15], and has also been used as the efficient sensitizer to extend the absorption spectra of oxide semiconductor photocatalysts from the UV region into visible region [16–18]. More recently, a new type of polymeric nanosheet structure, graphitic carbon nitride (g-C_3N_4), has been introduced as a visible-light photocatalyst for water splitting due to its unique electronic band structure with high thermal and chemical stability [19–21].

In the development of semiconductor-based photocatalysts for solar-to-fuel conversion, one disconcerting drawback is the high recombination rate of photogenerated electron–hole pairs in the individual semiconductor structure [22]. Thus it is very critical to modulate the charge carrier dynamics in semiconductor structures.

One effective way is coupling two semiconductor units with appropriate band alignment between the two units to allow interfacial charge transfer upon excitation and promote the separation efficiency of photogenerated electrons and holes [23–29]. Thus the charge carrier lifetime can be significantly improved to enable desired surface reactions and thereby enhance the photocatalytic efficiency for solar-to-fuels conversion.

Recently researchers have found that two-dimensional (2-D) semiconductor nanostructures offer higher charge mobility and lower recombination rates of charge carriers as compared to 0-D spherical nanoparticles [30,31]. Herein, we present a prototype of 0D–2D semiconductor heterojunction system by in-situ growth of In_2O_3 nanocrystals on g-C_3N_4 nanosheets through a simple solvothermal method. The well-dispersed In_2O_3 nanocrystals on sheet-like g-C_3N_4 surfaces form intimate contact, which allows for effective interfacial charge transfer across the In_2O_3/g-C_3N_4 heterojunction since the conduction band (CB) and valance band (VB) positions of In_2O_3 (~−0.6 eV and ~+2.2 eV, respectively, vs. NHE) [28,29] are both lower than those of g-C_3N_4 (~−1.1 eV and ~+1.6 eV, respectively, vs. NHE) [19,32]. In particular, the conduction band edge (~−0.6 eV) of In_2O_3 is high enough for reduction of proton and CO_2. As such, we found that the In_2O_3/g-C_3N_4 hybrid structures are capable for efficient photocatalytic H_2 generation and CO_2 reduction with much higher activities than the pure In_2O_3 and g-C_3N_4. This is attributed to the highly effective charge separation on In_2O_3/g-C_3N_4 hybrids as confirmed by the transient photoluminescence (PL) spectroscopy.

2. Experiments

2.1. Preparation of In₂O₃–g-C₃N₄ hybrids

g-C₃N₄ powder was synthesized by heating 6 g melamine in an alumina crucible with a cover at 500 °C in a muffle furnace for 2 h at a heating rate of 20 °C/min, and further heated to 520 °C for another 2 h at a heating rate of 5 °C/min [33]. In-situ growth of In₂O₃ nanocrystals (10 wt%) on g-C₃N₄ nanosheets was carried out as following steps. While stirring, 0.5 mmol of In(Ac)₃ and 600 mg of the as-prepared g-C₃N₄ were added into 50 mL dimethyl sulfoxide (DMSO). The resultant suspension was sealed in a 100 mL teflon-lined stainless-steel autoclave. The autoclave was heated to 180 °C and maintained for 12 h, and then allowed to cool to room temperature. The product was collected after centrifugation, washed with water and ethanol repeatedly, and then dried in a vacuum oven. Pure In₂O₃ and other In₂O₃–g-C₃N₄ hybrids with different ratio were synthesized using the similar route by tuning the dosage of g-C₃N₄.

2.2. Characterization

A Shimadzu XRD-6000 X-ray diffractometer (Cu $K\alpha$ source) was used to record X-ray powder diffraction (XRD) patterns with the 2θ range from 5 to 80° at a scan rate of 1°/min. Transmission electron microscopy (TEM) images were obtained from a JEOL JEM-2100F transmission electron microscope at an accelerating voltage of 200 kV. UV–vis diffuse reflectance spectra (DRS) were taken with a Lambda 750 UV/Vis/NIR spectrophotometer (Perkin Elmer, USA). X-ray photoelectron spectroscopy (XPS) measurement was performed on a thermo scientific theta probe XPS with monochromatized Al $K\alpha$ ($h\nu$ = 1486.6 eV) source. The steady-state photoluminescence (PL) spectra were obtained by a Shimazu RF-5310PC fluorometer at an excitation wavelength of 325 nm.

2.3. Transient optical spectroscopy

For time-resolved PL measurements, the excitation pulse (325 nm) was generated from an optical parametric amplifier (TOPAS™, Light Conversion Ltd). The time-resolved PL spectra were obtained using a streak camera (Optronics GmbH) with a time resolution of 10 ps. The PL decay profile is fitted by using multiexponential function [34,35].

$$I_t = \sum_{i=1}^{n} A_i \exp\left(-\frac{t}{\tau_i}\right)$$

where I_t is intensity, A_i is the relative magnitude of the ith decay and τ_i is the ith decay time.

2.4. Photocatalytic hydrogen evolution

Typically, 5 mg of the prepared photocatalysts were suspended in 10 mL aqueous solution of 0.1 M L-ascorbic acid (pH = 4.0). Pt cocatalyst (0.5 wt%) was in-situ loaded by adding 61 μL of H₂PtCl₆ (0.08 wt%) aqueous solution into the suspension followed by the irradiation of a 300-W xenon lamp (MAX-302, Asahi Spectra, USA) coupled with a UV cut-off filter (λ > 420 nm). The suspension was then purged with argon to drive away the residual air before sealed in a quartz flask. The photocatalytic hydrogen evolution was carried out by irradiating the suspension with a 300-W xenon lamp (MAX-302, Asahi Spectra, USA) coupled with a UV cut-off filter (λ > 420 nm). The output light intensity is 200 mW/cm². The gas product composition was analyzed periodically by an Agilent 7890A gas chromatograph (GC) with TCD detector.
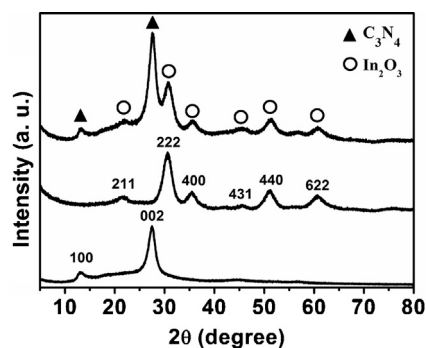

Fig. 1. XRD patterns of g-C₃N₄, In₂O₃, and 10 wt% In₂O₃–g-C₃N₄.

2.5. Photocatalytic CO₂ reduction

In the photocatalytic reduction of CO₂, 20 mg of the sample was uniformly dispersed on a glass substrate with a base area of 2.5 × 2.5 cm², which was then put into a quartz reactor (90 mL). Prior to irradiation, the reactor was purged with high-purity CO₂ gas and 0.1 mL ultrapure water was injected into the reactor. A 500-W Xenon lamp (Newport, USA) with output light intensity of 1200 mW/cm² was used as the light source for the photocatalytic reaction. During the irradiation, the gas product was taken from the reaction cell at given intervals to quantitatively analyze gas product composition by an Agilent 7890A gas chromatograph (GC) with TCD detector.

2.6. Photoelectrochemical measurements

Photocurrent measurements were performed on an electrochemical workstation (CHI852c, CH Instruments) with a three-electrode configuration. Our sample, Ag/AgCl electrode, and Pt-wire electrode were employed as the working, reference, and counter electrode, respectively. Irradiation was carried out by using a 300-W xenon lamp (MAX-302, Asahi Spectra, USA) coupled with a UV cut-off filter (λ > 420 nm) and an output intensity of 200 mW/cm². The Na₂SO₄ solution (0.1 M) was used as the electrolyte. The working electrodes were prepared by spreading aqueous slurries of various samples on FTO glass substrate, using adhesive tapes as spaces to obtain a 1 cm × 1 cm electrode. The applied bias was set as 0.4 V.

3. Results and discussion

The XRD patterns of the as-prepared g-C₃N₄, In₂O₃, and In₂O₃–C₃N₄ hybrids (10 wt% In₂O₃) are shown in Fig. 1. Two pronounced diffraction peaks locate at 27.4° and 13.1° for g-C₃N₄, which could be ascribed to the characteristic interlayer stacking peak of aromatic systems as the (0 0 2) peak for graphitic materials, and the interplanar separation as the (1 0 0) peak, respectively [33,36]. The XRD pattern of In₂O₃ gives rise to six distinct diffraction peaks at 21.5°, 30.6°, 35.6°, 45.4°, 50.9°, and 60.8°, which can be attributed to the (2 1 1), (2 2 2), (4 0 0), (4 3 1), (4 4 0), and (6 2 2) crystal planes of cubic In₂O₃ (JCPDS No. 71-2194), respectively. The In₂O₃–g-C₃N₄ hybrids exhibit characteristic XRD peaks of both In₂O₃ and g-C₃N₄.

TEM and SEM images (Fig. 2) are taken to directly analyze the structures of the samples. Fig. 2a indicates that the polymeric g-C₃N₄ has a sheet-like structure. The pure In₂O₃ sample prepared without g-C₃N₄ is shown as nanoparticle aggregation (Fig. 2b). However, in the presence of g-C₃N₄, the solvethermal process generated small In₂O₃ nanocrystals well spreading on the g-C₃N₄ surface, as shown by Fig. 2c. The HRTEM image (Fig. 2d) confirms the existence of small In₂O₃ nanocrystals, and the lattice fringes
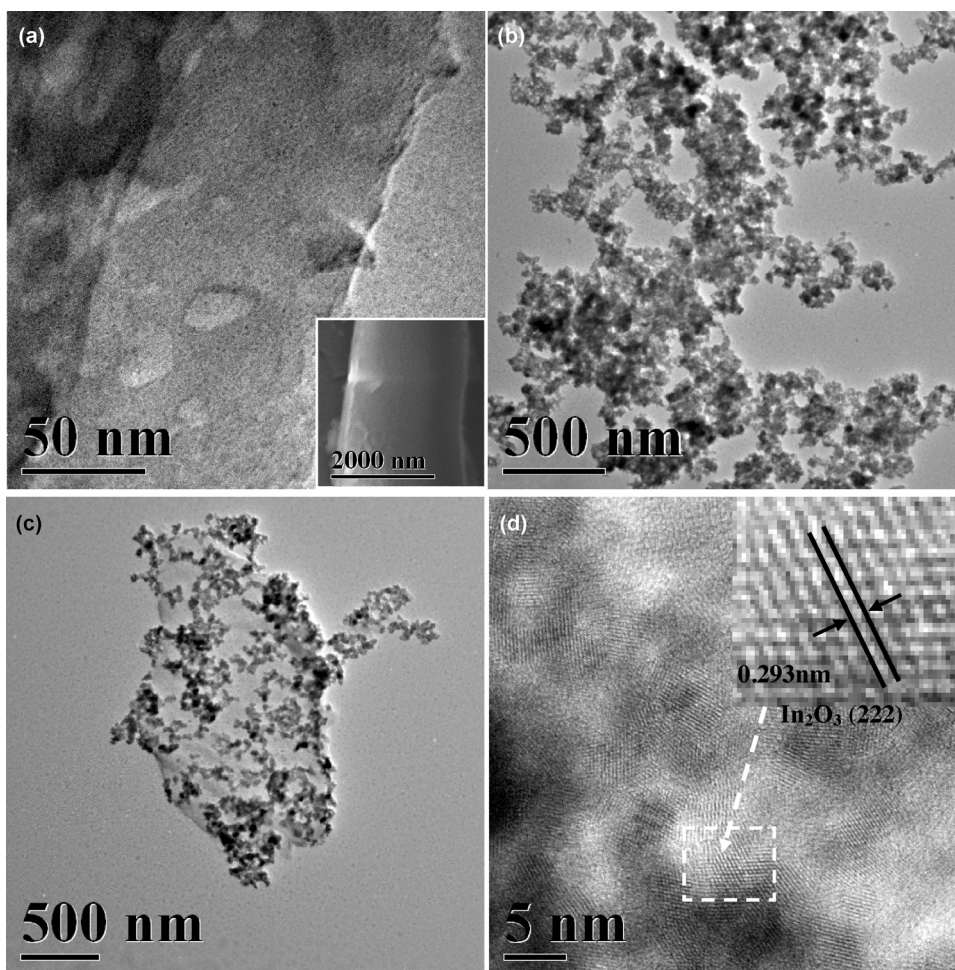
Fig. 2. TEM image of (a) g-C₃N₄; (b) In₂O₃; and (c) 10 wt% In₂O₃–g-C₃N₄; (d) HRTEM image of 10 wt% In₂O₃–g-C₃N₄. Inset of Fig. 2a is the SEM image of g-C₃N₄.

with d spacing of 0.293 nm can be assigned to the (2 2 2) crystal plane of cubic In_2O_3.

Fig. 3 shows the absorption spectra of the prepared g-C₃N₄, In_2O_3, and In_2O_3–g-C₃N₄ hybrid (10 wt% In_2O_3). The pure g-C₃N₄ and In_2O_3 samples presented a similar absorption edge at ∼450 nm with wide overlap between their absorption spectra, thereby the absorption feature of the In_2O_3–g-C₃N₄ hybrids showed very little difference with that of pure g-C₃N₄. We further examine the In_2O_3–g-C₃N₄ hybrid (10 wt% In_2O_3) through XPS. As shown in Fig. 4a, the peak of C 1s binding energies at 284.6 eV and 288.2 eV can be ascribed to sp² C–C bonds and sp²-bonded carbon in N-containing aromatic rings (N–C=N), respectively, which are the
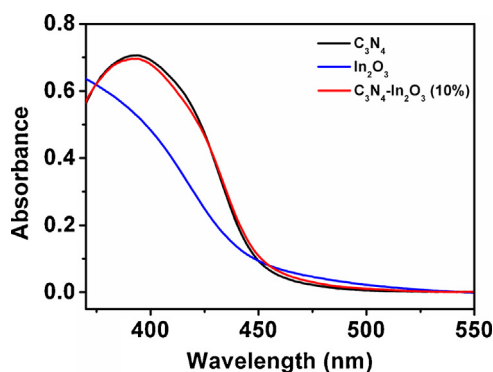
major carbon species in the g-C₃N₄ [37,38]. The weak shoulder that can be deconvoluted into a peak at 285.8 eV could be assigned to sp³-coordinated carbon bonds from the defects on g-C₃N₄ surface [21,36]. The N 1s spectrum showed two clear peaks (Fig. 4b) at 398.7 eV and 401.1 eV, corresponding to sp²-bonded N involved in the triazine rings (C–N=C) and amino groups (C–N–H); and the tiny shoulder between these two peaks can be deconvoluted into a peak at 399.8 eV caused by the tertiary nitrogen N–(C)₃ groups [39,40]. The binding energies of In 3d locate at 444.4 and 451.9 eV (Fig. 4c), which can be assigned to the In^{3+} in In_2O_3 nanocrystals [29,41]. The O 1s peaks at 529.7 and 531.5 eV (Fig. 4d) can be assigned to the oxygen in In_2O_3 nanocrystals.

Photocatalytic activities of the prepared samples for hydrogen evolution under visible light (λ > 420 nm) irradiation were evaluated by using L-ascorbic acid as the sacrificial reagent to consume photoinduced holes, and 0.5 wt% Pt was in-situ deposited as cocatalyst onto the samples to reduce the overpotential of H_2 evolution. L-ascorbic acid has been proved as an effective water soluble electron donor since its ascorbate anion can function as reductive quencher and also allows for the incorporation of a large amount of L-ascorbic acid in the aqueous reaction system [42–44]. Fig. 5a shows the H_2 evolution plots by g-C₃N₄, In_2O_3, and In_2O_3–g-C₃N₄ hybrids (10 wt% In_2O_3) as a function of irradiation time. The pure In_2O_3 sample did not show noticeable H_2 evolution, and the pure g-C₃N₄ showed a H_2 generation rate of 0.19 μmol/h. Remarkably, when 10 wt% In_2O_3 nanocrystals are decorated on g-C₃N₄ surfaces, the hybrid structure exhibited five times higher H_2 generation rate (0.99 μmol/h) than the pure g-C₃N₄.

Fig. 3. UV–vis absorption spectra of g-C₃N₄, In_2O_3, and 10 wt% In_2O_3–g-C₃N₄.
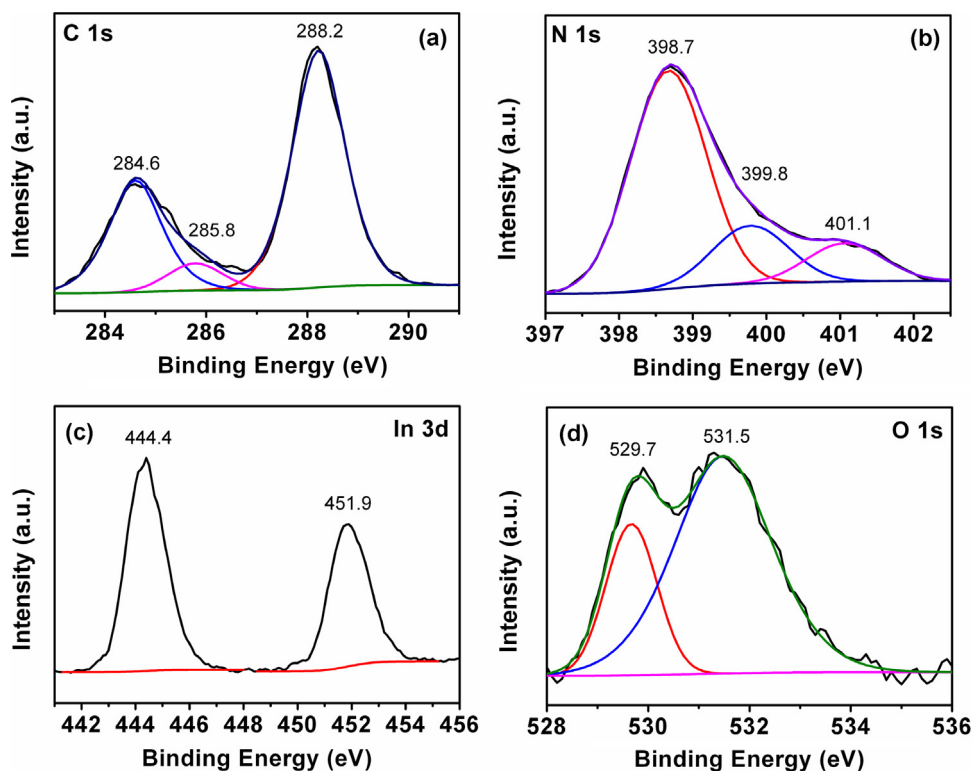
Fig. 4. XPS spectra of 10 wt% In_2O_3–g-C_3N_4: (a) C 1s; (b) N 1s; (c) In 3d; (d) O 1s.

However, the decoration content of In_2O_3 showed considerable influence on the photocatalytic activity of the In_2O_3–g-C_3N_4 hybrids. Even with small amount of In_2O_3 (2.5 wt%) nanocrystals on g--C_3N_4 surfaces, the H_2 evolution amount can be 2.4 times higher than that of pure g-C_3N_4. As shown in Fig. 5b, the photocatalytic activity of the In_2O_3–g-C_3N_4 hybrids increases with more H_2 generation as the In_2O_3 content rise to 10 wt%. However, excessive In_2O_3 nanocrystals (>10 wt%) grown on g-C_3N_4 surfaces led to decreased photocatalytic activity in H_2 generation, which might be due to the aggregation of In_2O_3 nanocrystals. As shown in Fig. 6a, in the hybrid sample with 20 wt% In_2O_3, excess In_2O_3 nanocrystals are aggregating on the g-C_3N_4 surface, which reduces the interface area between In_2O_3 and g-C_3N_4 and thereby lower the charge separation efficiency relying on interfacial electron transfer. In addition, over-coverage of In_2O_3 may reduce reactive sites on g-C_3N_4 surfaces that are needed to quench the holes. This would also cause decreased photocatalytic activity. In short, our observation indicates that the optimal decoration amount of In_2O_3 nanocrystals is 10 wt% to obtain the highest photocatalytic activity for H_2 generation. We further explore the stability of the optimal In_2O_3–g-C_3N_4 hybrids (10 wt% In_2O_3) by a four-run cycling test of photocatalytic hydrogen evolution. Fig. 6b reveals that no obvious decrease of H_2 evolution was observed after the four cycles under 16-h visible light irradiation, suggesting the excellent stability of the In_2O_3–g-C_3N_4 hybrids in the reactions.

In order to further demonstrate the improved photocatalytic activity by the in-situ grown In_2O_3 nanocrystals on g-C_3N_4, the prepared samples were evaluated by using reaction of photocatalytic CO_2 reduction into hydrocarbon fuels that is known as a challenging but promising application for sustainable energy resources [45–47]. As shown in Fig. 7a, after 4-h irradiation, the optimal In_2O_3–g-C_3N_4 hybrids with 10 wt% In_2O_3 exhibited a CH_4 production yield of 76.7 ppm (over 20 mg samples) without any cocatalyst, which is more than three times higher than that of pure g-C_3N_4 and more than four times higher than that of pure In_2O_3. The influence of In_2O_3 loading content on the CH_4 production yield showed a
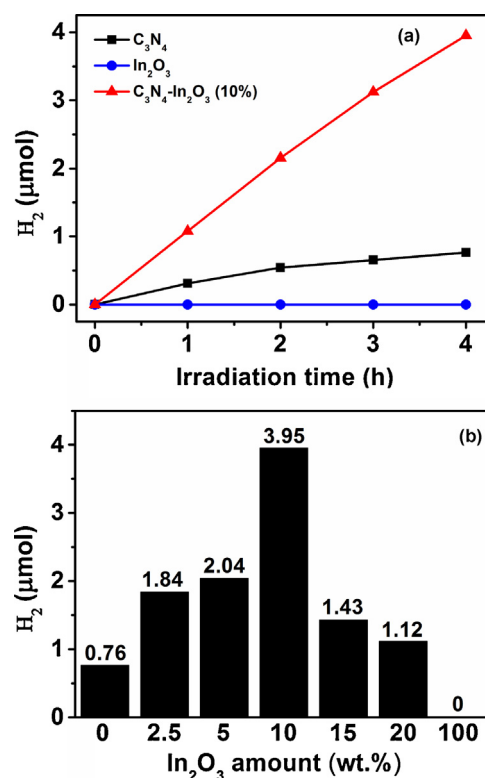

Fig. 5. (a) Plots of photocatalytic H_2 evolution amount versus irradiation ($\lambda > 420$ nm) time for different samples (5 mg); (b) comparison of H_2 evolution amount over different samples (5 mg) after visible light irradiation for 4 h.

similar trend with that on photocatalytic H_2 generation. Note that these tests of photocatalytic CO_2 reduction were carried out without loading any cocatalyst. Indeed, if we photo-deposited 0.5 wt% Pt-cocatalyst onto the In_2O_3–g-C_3N_4 hybrids (10 wt% In_2O_3), the
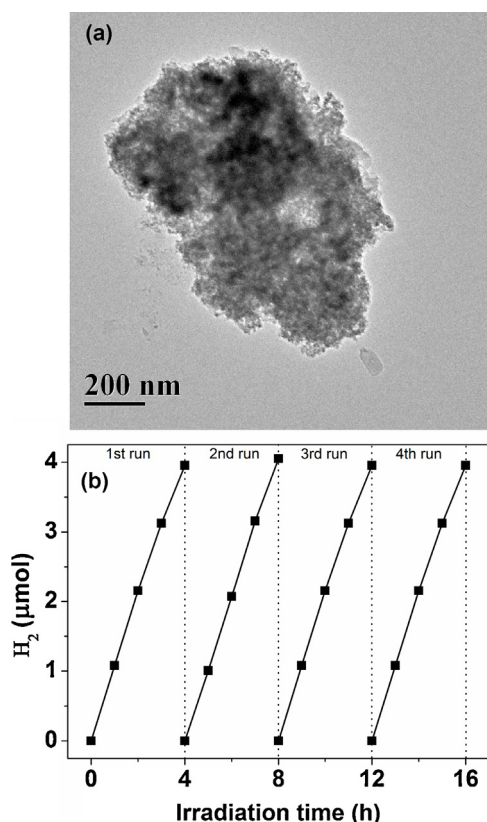
Fig. 6. (a) TEM image of 20 wt% In$_2$O$_3$–g-C$_3$N$_4$; (b) cycling test of photocatalytic H$_2$ evolution for 10 wt% In$_2$O$_3$–g-C$_3$N$_4$.
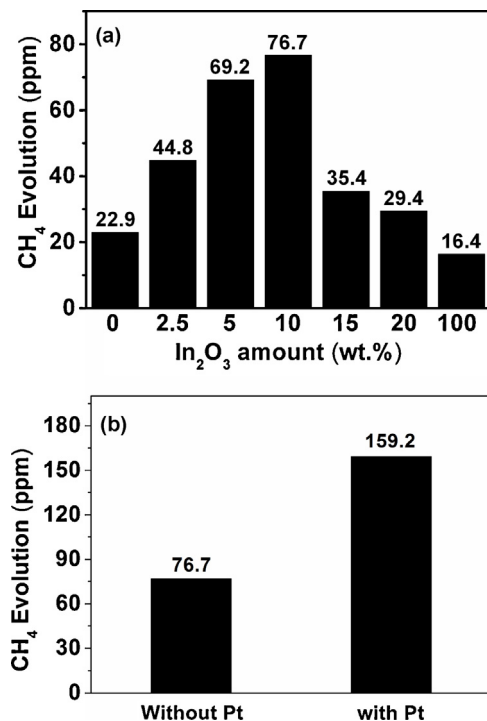

Fig. 7. Comparison of CH$_4$ production amount from photocatalytic CO$_2$ reduction after 4-h UV–vis irradiation (a) over different samples (20 mg) without any cocatalyst; (b) over 10 wt% In$_2$O$_3$–g-C$_3$N$_4$ (20 mg) with and without Pt loading.
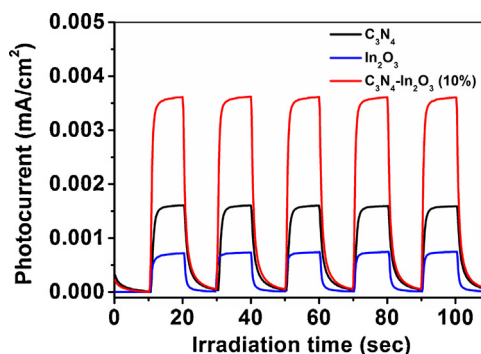

Fig. 8. Transient photocurrent responses for the g-C$_3$N$_4$, In$_2$O$_3$, and 10 wt% In$_2$O$_3$–g-C$_3$N$_4$ samples.

Table 1
Fitted lifetimes of the fluorescence decay profiles from Fig.9b.

Species	A_1 (%)	τ_1 (ns)	A_2 (%)	τ_2 (ns)
C$_3$N$_4$	–	–	100	3
In$_2$O$_3$–C$_3$N$_4$	54.7	0.71	45.3	3

CH$_4$ production yield could be further promoted to 159.2 ppm upon 4-h irradiation. This indicates that in the photocatalytic CO$_2$ reduction, the Pt cocatalyst still can act as electron sinks to effectively improve the charge separation of the In$_2$O$_3$–g-C$_3$N$_4$ hybrid structure.

We also carried out the photoelectrochemical measurements to obtain the transient photocurrent responses for the samples of g-C$_3$N$_4$, In$_2$O$_3$, and 10 wt% In$_2$O$_3$–g-C$_3$N$_4$ under several on-off cycles of irradiation. As shown in Fig. 8, The In$_2$O$_3$–g-C$_3$N$_4$ hybrid sample shows the highest photocurrent intensity among the three samples. This observation indicates that the formed In$_2$O$_3$–g-C$_3$N$_4$ heterojunctions allow for the more efficient separation of photogenerated electron–hole pairs as compared to the individual g-C$_3$N$_4$ and In$_2$O$_3$.

On the basis of the above experimental results, we believe that the enhanced photocatalytic activities by the in-situ grown In$_2$O$_3$ nanocrystals are attributed to the interfacial transfer of photogenerated electrons and holes between g-C$_3$N$_4$ and In$_2$O$_3$, which leads to effective charge separation on both parts. To further prove this assumption, we performed measurements by using both steady-state and transient photoluminescence (PL) spectroscopy. Fig. 9a shows that at an excitation wavelength of 325 nm, the pure g-C$_3$N$_4$ sample exhibits a strong emission peak centered at ~450 nm. In comparison, when 10 wt% In$_2$O$_3$ nanocrystals were present on the g-C$_3$N$_4$ surface, the intensity of this emission band dropped significantly, indicating efficient transfer of photoexcited electrons from g-C$_3$N$_4$ to In$_2$O$_3$ nanocrystals. The lifetime of charge carriers in the In$_2$O$_3$–g-C$_3$N$_4$ hybrids (10 wt% In$_2$O$_3$) were examined by using time-resolved transient PL spectroscopy, as shown in Fig. 9b. The fitted lifetimes of the PL decay profile are listed in Table 1. The pure g-C$_3$N$_4$ sample exhibits only one radiative lifetime of 3 ns, which is associated with the photoexcited electrone–hole pairs in g-C$_3$N$_4$ that eventually undergo recombination [48]. While for the In$_2$O$_3$–g-C$_3$N$_4$ hybrids, a shorter PL lifetime component ($\tau_1 = 0.71$ ns with a weighing factor $A_1 = 54.7$%) appears, suggesting that some excited electrons undergo rapid transfer from g-C$_3$N$_4$ to In$_2$O$_3$. This evidence of fast electron-injection confirms that the formation of In$_2$O$_3$–g-C$_3$N$_4$ heterostructures remarkably promotes charge transfer efficiency, thereby favoring the photocatalytic reactions for H$_2$ evolution and CO$_2$ reduction.

Fig. 10 shows the schematic illustration of the possible photocatalytic mechanism. The enhanced photocatalytic activity could be attributed to the effective interfacial charge transfer between
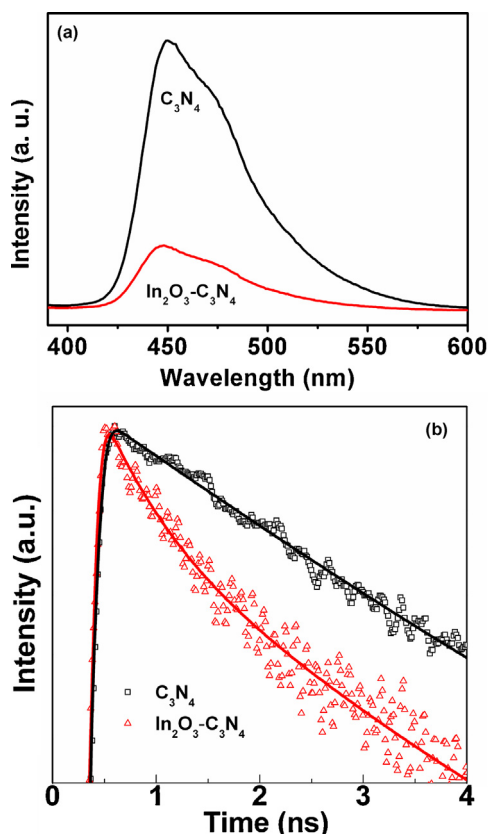
Fig. 9. (a) Steady-state PL spectra and (b) time-resolved transient PL decay for pure g-C_3N_4 and the 10 wt% In_2O_3–g-C_3N_4.

In_2O_3 and g-C_3N_4 across the heterojunction. Since the CB of g-C_3N_4 (~−1.1 eV vs. NHE) is more negative than that of In_2O_3 (~−0.6 eV vs. NHE), the photoexcited electrons on the CB of g-C_3N_4 can rapidly transfer to the CB of In_2O_3. These accumulated electrons, together with the electrons excited from the VB of In_2O_3, are capable of reducing H^+ and/or CO_2 into valuable fuels. While the corresponding VB position of In_2O_3 (~+2.2 eV vs. NHE) is more positive than that of g-C_3N_4 (~+1.6 eV vs. NHE), the photogenerated holes on the VB of In_2O_3 can migrate to the VB of g-C_3N_4, subsequently to oxidize the electron donor (ascorbic acid for H_2 production and OH^- for CO_2 reduction, respectively). As such, effective charge separation can be achieved, resulting in longer lifetime of the photogenerated charge carriers and thereby enhanced photocatalytic activities.
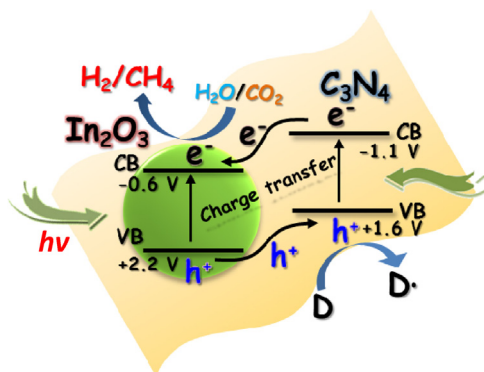

Fig. 10. Schematic illustration of the photocatalytic process for H_2 evolution and CO_2 reduction on the In_2O_3–g-C_3N_4 nanohybrids.

4. Conclusions

In summary, we have successfully prepared In_2O_3/g-C_3N_4 hybrid structures through a simple solvothermal method. A small amount of In_2O_3 nanocrystals grown onto g-C_3N_4 surfaces leads to considerable improvement on the photocatalytic activities for H_2 evolution and CO_2 reduction. The enhanced activities are attributed to the effective interfacial charge transfer across the In_2O_3/g-C_3N_4 heterojunction, as evidenced by steady-state and transient PL studies. This work provides a new insight on developing 0D–2D semiconductor hetero-structured systems with effective charge separation for highly efficient solar-to-fuels conversion.

Acknowledgments

References

[1] H. Tong, S.X. Ouyang, Y.P. Bi, N. Umezawa, M. Oshikiri, J.H. Ye, Advanced Materials 24 (2012) 229–251.
[2] A. Kudo, Y. Miseki, Chemical Society Reviews 38 (2009) 253–278.
[3] L. Ge, C.C. Han, Applied Catalysis B: Environmental 117–118 (2012) 268–274.
[4] Z.Y. Yin, Z. Wang, Y.P. Du, X.Y. Qi, Y.Z. Huang, C. Xue, H. Zhang, Advanced Materials 24 (2012) 5374–5378.
[5] M. Tahir, N.S. Amin, Applied Catalysis B: Environmental 142 (2013) 512–522.
[6] S. Somasundaram, C.R.N. Chenthamarakshan, N.R. De tacconi, K. Rajeshwar, International Journal of Hydrogen Energy 32 (2007) 4661–4669.
[7] P.D. Tran, S.K. Batabyal, S.S. Pramana, J. Barber, L.H. Wong, S.C. Loo, Nanoscale 4 (2012) 3875–3878.
[8] S.X. Ouyang, H. Tong, N. Umezawa, J.Y. Cao, P. Li, Y.P. Bi, Y.J. Zhang, J.H. Ye, Journal of the American Chemical Society 134 (2012) 1974–1977.
[9] S. Hara, H. Irie, Applied Catalysis B: Environmental 115–116 (2012) 330–335.
[10] H. Lv, L. Ma, P. Zeng, D. Ke, T. Peng, Journal of Materials Chemistry 20 (2010) 3665–3672.
[11] B. Girginer, G. Galli, E. Chiellini, N. Bicak, International Journal of Hydrogen Energy 34 (2009) 1176–1184.
[12] Q.J. Xiang, B. Cheng, J.G. Yu, Applied Catalysis B: Environmental 138–139 (2013) 299–303.
[13] S.W. Cao, J. Fang, M.M. Shahjamali, F.Y.C. Boey, J. Barber, S.C.J. Loo, C. Xue, RSC Advances 2 (2012) 5513–5515.
[14] F. Quarto, C. Sunseri, S. Piazza, M. Romano, Journal of Physical Chemistry B 101 (1997) 2519–2525.
[15] Z.M. Li, P.Y. Zhang, T. Shao, X.Y. Li, Applied Catalysis B: Environmental 125 (2012) 350–357.
[16] W.K. Chang, K.K. Rao, H.C. Kuo, J.F. Cai, M.S. Wong, Applied Catalysis A: General 321 (2007) 1–6.
[17] Z.Y. Wang, B.B. Huang, Y. Dai, X.Y. Qin, X.Y. Zhang, P. Wang, H.X. Liu, J.X. Yu, Journal of Physical Chemistry C 113 (2009) 4612–4617.
[18] J. Lv, T. Kako, Z.S. Li, Z.G. Zou, J.H. Ye, Journal of Physical Chemistry C 114 (2010) 6157–6162.
[19] X.C. Wang, K. Maeda, A. Thomas, K. Takanabe, G. Xin, J.M. Carlsson, K. Domen, M. Antonietti, Nature Materials 8 (2009) 76–80.
[20] K. Maeda, X.C. Wang, Y. Nishihara, D. Lu, M. Antonietti, K. Domen, Journal of Physical Chemistry C 113 (2009) 4940–4947.
[21] G.G. Zhang, J.S. Zhang, M.W. Zhang, X.C. Wang, Journal of Materials Chemistry 22 (2012) 8083–8091.
[22] X.B. Chen, S.H. Shen, L.J. Guo, S.S. Mao, Chemical Reviews 110 (2010) 6503–6570.
[23] D. Sarkar, C.K. Ghosh, S. Mukherjee, K.K. Chattopadhyay, ACS Applied Materials & Interfaces 5 (2013) 331–337.
[24] H.W. Bai, J. Juay, Z.Y. Liu, X.X. Song, S.S. Lee, D.D. Sun, Applied Catalysis B: Environmental 125 (2012) 367–374.
[25] L.L. Xu, J.G. Guan, W.D. Shi, L.J. Liu, Journal of Colloid and Interface Science 377 (2012) 160–168.
[26] M. Moriya, T. Minegishi, H. Kumagai, M. Katayama, J. Kubota, K. Domen, Journal of the American Chemical Society 135 (2013) 3733–3735.
[27] Y.P. Yuan, S.W. Cao, Y.S. Liao, L.S. Yin, C. Xue, Applied Catalysis B: Environmental 140–141 (2013) 164–168.
[28] Y.C. Chen, Y.C. Pu, Y.J. Hsu, Journal of Physical Chemistry C 116 (2012) 2967–2975.
[29] J.B. Mu, B. Chen, M.Y. Zhang, Z.C. Guo, P. Zhang, Z.Y. Zhang, Y.Y. Sun, C.L. Shao, Y.C. Liu, ACS Applied Materials & Interfaces 4 (2012) 424–430.

[30] J. Zhang, J.G. Yu, Y.M. Zhang, Q. Li, J.R. Gong, Nano Letters 11 (2011) 4774–4779.
[31] F.K. Meng, Z.L. Hong, J. Arndt, M. Li, M.J. Zhi, F. Yang, N.Q. Wu, Nano Research 5 (2012) 213–221.
[32] S.C. Yan, S.B. Lv, Z.S. Li, Z.G. Zou, Dalton Transactions 39 (2010) 1488–1491.
[33] S.C. Yan, Z.S. Li, Z.G. Zou, Langmuir 25 (2009) 10397–10401.
[34] J.L. Wu, F.C. Chen, Y.S. Hsiao, F.C. Chien, P.L. Chen, C.H. Kuo, M.H. Huang, C.S. Hsu, ACS Nano 5 (2011) 959–967.
[35] B. Wu, T.Z. Oo, X.L. Li, X.F. Liu, X.Y. Wu, E.K.L. Yeow, H.J. Fan, N. Mathews, T.C. Sum, Journal of Physical Chemistry C 116 (2012) 14820–14825.
[36] S.W. Cao, Y.P. Yuan, J. Fang, M.M. Shahjamali, F.Y.C. Boey, J. Barber, S.C.J. Loo, C. Xue, International Journal of Hydrogen Energy 38 (2013) 1258–1266.
[37] Y. Wang, X. Wang, M. Antonietti, Angewandte Chemie International Edition 51 (2012) 68–89.
[38] A. Vinu, Advanced Functional Materials 18 (2008) 816–827.
[39] A. Thomas, A. Fischer, F. Goettmann, M. Antonietti, J.-O. Müller, R. Schlögl, J.M. Carlsson, Journal Materials Chemistry 18 (2008) 4893–4908.
[40] Q. Xiang, J. Yu, M. Jaroniec, Journal of Physical Chemistry C 115 (2011) 7355–7363.
[41] J.B. Mu, C.L. Shao, Z.C. Guo, M.Y. Zhang, Z.Y. Zhang, P. Zhang, B. Chen, Y.C. Liu, Journal of Materials Chemistry 22 (2012) 1786–1793.
[42] Y. Na, M. Wang, J.X. Pan, P. Zhang, B. Åkermark, L.C. Sun, Inorganic Chemistry 47 (2008) 2805–2810.
[43] S. Caramori, V. Cristino, R. Argazzi, L. Meda, C.A. Bignozzi, Inorganic Chemistry 49 (2010) 3320–3328.
[44] F. Wang, W.G. Wang, X.J. Wang, H.Y. Wang, C.H. Tung, L.Z. Wu, Angewandte Chemie International Edition 50 (2011) 3193–3197.
[45] H.F. Cheng, B.B. Huang, Y.Y. Liu, Z.Y. Wang, X.Y. Qin, X.Y. Zhang, Y. Dai, Chemical Communications 48 (2012) 9729–9731.
[46] X.Y. Chen, Y. Zhou, Q. Liu, Z.D. Li, J.G. Liu, Z.G. Zou, ACS Applied Materials & Interfaces 4 (2012) 3372–3377.
[47] H. Xu, S.X. Ouyang, P. Li, T. Kako, J.H. Ye, ACS Applied Materials & Interfaces 5 (2013) 1348–1354.
[48] V.I. Klimov, D.W. McBranch, C.A. Leatherdale, M.G. Bawendi, Physical Review B: Condensed Matter 60 (1999) 13740–13749.